




 Cite this: *RSC Adv.*, 2021, 11, 335

Effect of annealing on the defect-mediated blue phosphorescence in ZnO nanocrystals†

 Sagnik Das,^a Uttam Kumar Ghorai,^b Rajib Dey,^c Chandan Kumar Ghosh ^c and Mrinal Pal ^{*a}

Recently, UV/NUV excitable RGB phosphors with precisely tunable PL emission properties have been in high demand for their suitability in the fabrication of white LEDs. In this paper, we report to have tuned the PL intensity, shade, and color temperature of the defect-mediated blue phosphorescence of ZnO nanopowders by systematic annealing at different temperatures. The ZnO nanopowder was prepared by a facile and cost-effective aqueous solution-precipitation method. The as-synthesized nanopowder was annealed at different temperatures ranging from 150 °C to 850 °C and all these samples were characterized by XRD, FESEM, EDX, BET, Raman spectroscopy, and UV-Vis spectroscopy to have insight into their microstructural, compositional, and band-structure details. Optical studies of the samples were conducted by PL and τ -PL spectroscopy. Color coordinates of the samples were obtained from the CIE plots derived from the PL spectra. The CIE coordinates were further used to calculate the CCT values of the samples. τ -PL spectroscopy was carried out to measure the life-time of the photogenerated electrons. PL studies of the samples revealed that the blue emissions have red, yellow, and blue components originating from crystalline point defects, *viz.* zinc interstitial (Zn_i), and oxygen interstitial (O_i). Annealing at different temperatures triggered changes in the defect concentrations leading to the corresponding changes in the intensity, shade, and color temperature of the blue phosphorescence.

 Received 30th May 2020
 Accepted 13th December 2020

DOI: 10.1039/d0ra04766j

rsc.li/rsc-advances

Introduction

Phosphors are an important class of semiconductor and find applications in field emission displays (FED), flat panel displays, vacuum fluorescent displays (VFD), plasma display panels (PDP)^{1–5} *etc.* Recently, the most sought-after thing in the lighting industry has been white LEDs (W-LEDs). The commercial technique of producing W-LEDs is to combine blue LEDs (indium gallium nitride) with a yellow phosphor (Ce³⁺ doped yttrium aluminium garnet).⁶ However, this technique suffers from poor colour rendition, high CCT (>7000 K), and harmful effects of blue LEDs on the human eye and body.^{7–10} By far the best method for producing W-LEDs has been a combination of an ultraviolet/near ultraviolet (UV/NUV) LED with RGB phosphors.^{11–14} However, true whiteness in emission is achieved only when red, green, and blue colours are combined in correct proportions. This necessitates the development of phosphors with precise tunability in emission.

ZnO is an important optoelectronic material having a direct and wide (3.3 eV) band gap and large exciton binding energy (60 meV).^{15–17} Consequently, ZnO exhibits phosphorescence

originating from crystalline point defects, *viz.* oxygen vacancy, zinc vacancy, oxygen interstitial, zinc interstitial *etc.*^{18–24} Different approaches have been adopted in order to tune such defect-mediated phosphorescence by controlling the type and concentration of the crystalline defects. Recently, Rauwel *et al.* has reported on the precursor dependence of the defect mediated (oxygen vacancy and zinc interstitial/vacancy) blue-green PL emission in ZnO nanoparticles.²⁵ This study suggests that the type and concentration of the point defects in ZnO can be potentially tailored by the choice of appropriate precursors, thereby tuning the PL color and intensity. PL properties of ZnO can also be tuned by changing morphologies of the nanoparticles. For example, Gong *et al.* reported enhancement of PL emission in ZnO nanoparticles with rose-like morphology.²⁶ Singh *et al.* observed a quenching of PL emission with increasing rGO concentration in graphene-ZnO hybrid nanostructure.²⁷ Djurišić *et al.* and Zhang *et al.* reported that PL emission in ZnO can be manipulated by varying the excitation wavelength.^{28,29} Very recently, Garcia *et al.* reported that defect-mediated white phosphorescence in ZnGa₂O₄ can be controlled by modifying the annealing atmosphere.³⁰ In principle, it is possible to tune the defect concentration and hence the intensity, color/shade, and color temperature of phosphorescence in ZnO also by varying annealing temperature. However, any such systematic study can hardly be found in the prior art.

In this paper we have reported monotonic changes in the PL properties, *viz.* intensity, shade, life-time *etc.* of the defect-

^aCSIR-Central Glass and Ceramic Research Institute, Kolkata-700032, India. E-mail: palm@cgcri.res.in

^bRamakrishna Mission Vidyamandira, Howrah-711202, India

^cJadavpur University, Kolkata-700032, India

† Electronic supplementary information (ESI) available. See DOI: 10.1039/d0ra04766j



mediated blue phosphorescence in ZnO nanopowder by systematic annealing at different temperatures. ZnO nanopowder was prepared by a facile, and cost-effective solution-precipitation method. The as prepared nanopowder was annealed at seven different temperatures ranging from 150 °C to 850 °C in ordinary atmosphere. The nanopowders annealed at different temperatures were characterized by XRD (X-ray diffraction), FESEM (field emission scanning electron microscopy), EDX (Energy Dispersive X-ray), BET (Brunauer–Emmett–Teller), and micro-Raman spectroscopy to have an insight into the microstructure of the material. The photoluminescence emission spectra of all the samples revealed that the blue emissions were comprised of red, yellow, and blue components originating from crystalline point defects, *viz.* zinc interstitial (Zn_i), and oxygen interstitial (O_i). Plausible reaction mechanisms explaining their origins have been proposed. The concentrations of these defects and the intensities of the corresponding PL emission peaks varied as a function of annealing temperature. The corresponding CIE plots revealed that the shade of the emission gradually turned from light blue (CIE co-ordinate: (0.33, 0.30)) to dark blue (CIE co-ordinate: (0.27, 0.26)) as the annealing temperature increased from 150 °C to 850 °C. A thermodynamic interpretation to such variance in defect concentrations has been proposed. τ -PL study and correlated color temperature (CCT) calculations revealed phosphorescence and cool lighting in all the samples. Finally, all the samples exhibited quantum yields comparable to other ZnO based materials. This study suggests that this ZnO based blue phosphor owing to its tunable phosphorescence can be readily used for white LED fabrication. Further this study establishes thermal annealing as a technique for tuning of defect-mediated phosphorescence.

Experimental

Materials

Zinc nitrate hexahydrate ($Zn(NO_3)_2 \cdot 6H_2O$) (reagent grade, 98%, MW = 189.36 g mol⁻¹) and ammonium hydroxide (25%

ammonia solution) were procured from Sigma-Aldrich and E-merck, respectively. DI water was prepared in house.

Methods

ZnO nanoparticles were synthesized by a simple aqueous solution-precipitation route under ordinary atmosphere. 2.97 g of zinc nitrate hexahydrate (Merck) was dissolved in 100 ml of DI water and the solution was heated to 100 °C. To this solution 20 c.c. ammonium hydroxide (25% ammonia solution, Merck) was added dropwise until a pH of 10 was achieved. Thereafter, the solution was refluxed at 100 °C for 1 h in a flat bottom flask under continuous stirring at 1000 rpm. After 1 h, a dense white solid was precipitated. The precipitate was collected by centrifugation at 10 000 rpm for 10 minutes and dried at 80 °C for 5 h in ordinary atmosphere. This sample was annealed at different temperatures *viz.* 150 °C, 350 °C, 450 °C, 550 °C, 650 °C, 750 °C, and 850 °C under ordinary atmosphere for 3 h each. The annealed samples were designated as BZ150, BZ350, BZ450, BZ550, BZ650, BZ750, and BZ850, where BZ stands for 'Base ZnO' sample and the numerical values represent the annealing temperatures of the respective samples. Fig. 1 schematically illustrates the synthesis process. Additionally, BZ550-Ar and BZ550-O₂ samples were prepared by annealing the dried precipitate at 550 °C for 3 h in argon atmosphere and oxygen atmosphere, respectively.

Characterization

X-ray diffraction (XRD) patterns were recorded by Ultima III diffractometer (Cu K α radiation, $\lambda = 1.5404 \text{ \AA}$, Rigaku, Japan) to identify the phases present in the samples. Particle morphologies and elemental compositions of the samples were studied by field emission scanning electron microscopy and EDX study, respectively (FESEM, Hitachi S-4800). The specific surface area of the nanopowders were determined by BET study ((NovaWin, Quantachrome Instruments). For the FESEM analysis, samples were dispersed in isopropanol using an ultrasonic bath (250 W,

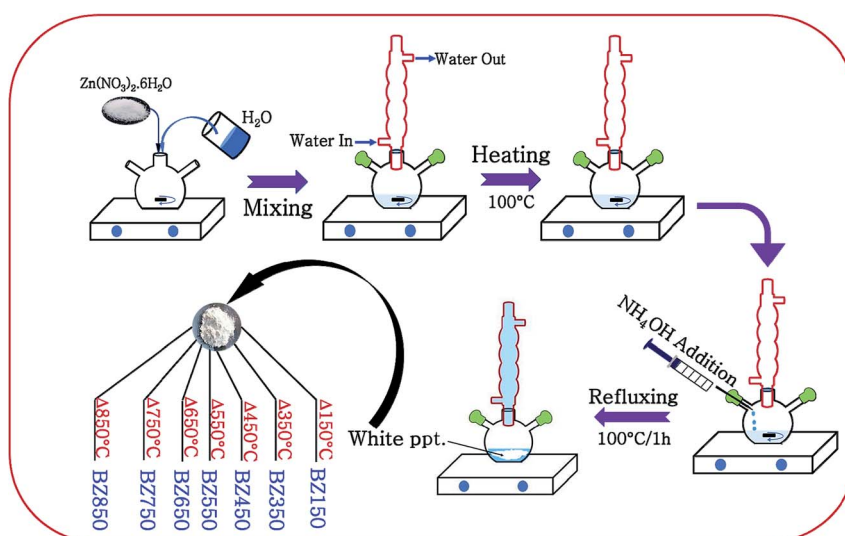


Fig. 1 Schematic illustration of the synthesis of BZ150, BZ350, BZ450, BZ550, BZ650, BZ750, and BZ850 samples.



Rivotek) and drop coated on hard aluminium foils. Room temperature micro-Raman spectroscopy of the samples was done using an alpha 300, WITEC, Germany having a laser source at 532 nm. Photoluminescence spectra were recorded at room temperature by using a spectrofluorometer (Edinburgh FLSP-980), having a Xe lamp source with an excitation wavelength of 300 nm to study the defect induced emission and their systematic variation in intensity with annealing temperature as the parameter. An Aquarius 7200 UV-Vis spectrometer was used to carry out the optical absorption study at room temperature. The Commission Internationale de l'Eclairage (CIE) coordinates were calculated for the emission spectrum which is the

superimposition of different emission spectra weighted to their concentrations. Lifetime of the photogenerated electrons for all the samples were investigated by an Edinburgh FLSP-980 make time resolved PL spectroscopic.

Results and discussion

Structural characterization

The XRD patterns of BZ150, BZ350, BZ450, BZ550, BZ650, BZ750, and BZ850 samples are shown in Fig. 2A. Several diffraction peaks at different positions are detectable from all the patterns. The crystallographic planes corresponding to

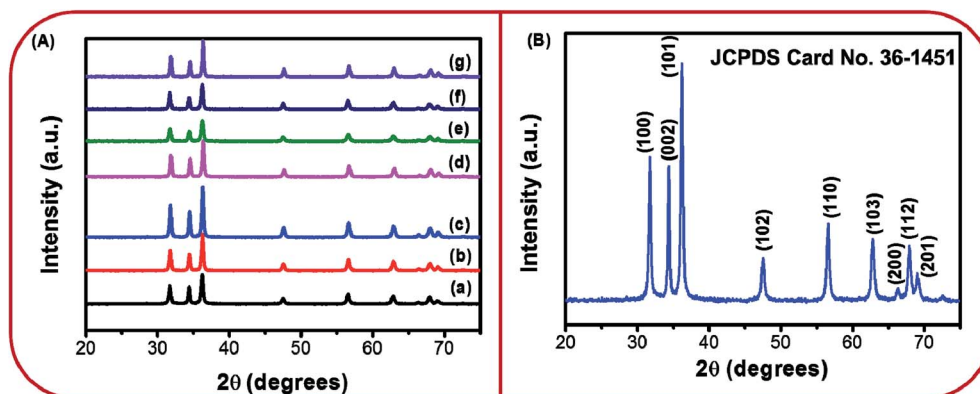


Fig. 2 (A) XRD patterns of (a) BZ150, (b) BZ350, (c) BZ450, (d) BZ550, (e) BZ650, (f) BZ750, (g) BZ850, and (B) XRD pattern of BZ150 with detectable crystallographic planes marked on it.

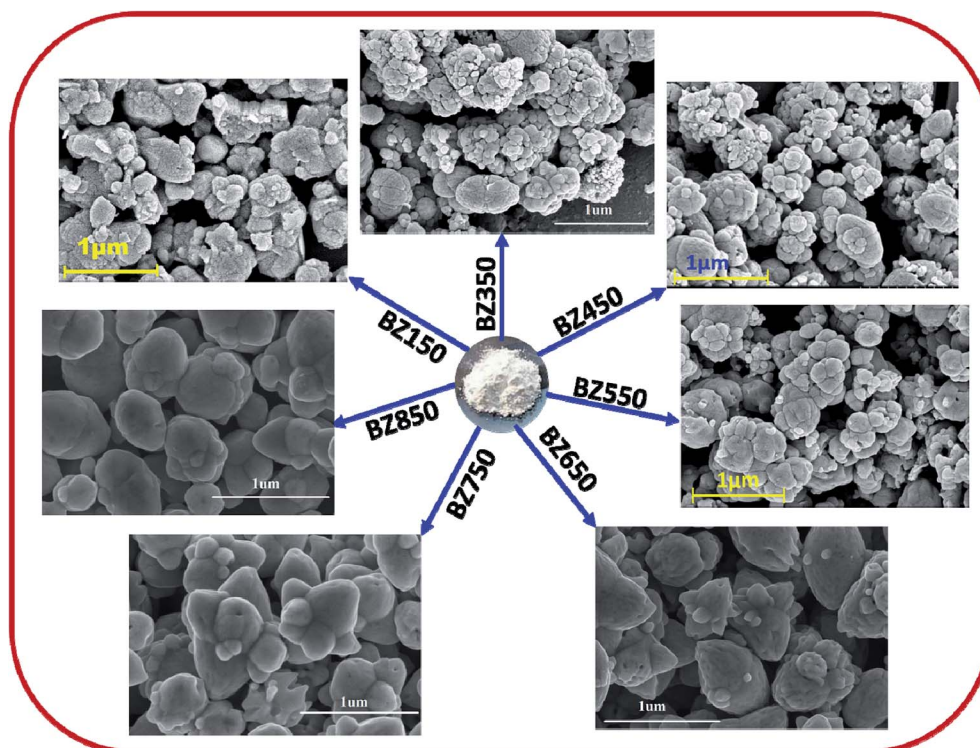


Fig. 3 FESEM images of BZ150, BZ350, BZ450, BZ550, BZ650, BZ750, and BZ850 samples.



these peaks have been marked on the diffraction pattern of BZ150 and shown in Fig. 2B. All the peak positions match well with the wurtzite ZnO (JCPDS card no. 36-1451).

No extra peak suggestive of any impurity is there. Sharp peaks observed in the XRD pattern indicate highly crystalline nature of prepared ZnO nanopowder. The average crystallite sizes of BZ150, BZ350, BZ450, BZ550, BZ650, BZ750, and BZ850 samples as calculated from the Scherrer equation are found to be 27 nm, 29 nm, 32 nm, 31 nm, 25 nm, 28 nm, and 34 nm, respectively.

Fig. 3 shows the typical FESEM images of all the samples. From the images it is clear that the particles are agglomerated to some extent. In spite of agglomeration cauliflower like morphology is visible in the FESEM images of the BZ150, BZ350, BZ450, BZ550, BZ650 and BZ750 samples. However, BZ850 sample shows spherical to extended spherical morphologies. Also, the particle sizes of BZ150, BZ350, BZ450 and BZ550 samples are in the range of 50–500 nm *i.e.* a wide variation of particle size can be observed. However, in BZ650, BZ750, and BZ850 samples comprise of mostly large (~500 nm) particles and small particles have almost disappeared. This indicates that at temperatures higher than 550 °C Ostwald ripening starts eliminating the smaller particles and above 750 °C sintering starts changing the cauliflower like particles into spherical ones.

Zn-to-O ratio for three representative samples, *viz.* BZ150, BZ550, and BZ850 have been determined by EDX study (ref. ESI-Fig. I† for EDX spectrums) and listed in Table 1. The Zn-to-O ratio increases from ~0.59 in BZ150 to ~0.85 in BZ850. The Zn to O ratio is less than one in each case. This clearly suggests the presence of oxygen interstitial (O_i) defects in all the samples. Further, this is also suggestive of the gradual annihilation of the oxygen interstitial (O_i) defects with increase in annealing temperature, especially at higher temperatures.

It was further observed that the Zn-to-O ratio in BZ550-Ar, BZ550, and BZ550-O₂ are ~0.70, ~0.67, and ~0.59, respectively (ref. Table 1). It is expected that with the increase in oxygen partial pressure in the annealing atmosphere, the removal of oxygen interstitial defect would reduce and this has been reflected in the reduction of Zn to O ratio with increasing oxygen partial pressure in the annealing atmosphere. No extra peak for any impurity element in the samples is observed in the EDX spectra (Au peaks are present as gold was sputtered on the samples for conducting FESEM and EDX studies) and this is in agreement with the XRD spectra of the samples (ref. Fig. 2) showing no peaks other than wurtzite ZnO.

Table 1 Elemental analysis of BZ150, BZ550-Ar, BZ550, BZ550-O₂, and BZ850 samples

Sample	Zn (atomic%)	O (atomic%)	Zn/O atomic ratio
BZ150	37.18	62.82	0.59
BZ550-Ar	41.38	58.62	0.70
BZ550	40.16	59.84	0.67
BZ550-O ₂	37.43	62.57	0.59
BZ850	46.13	53.87	0.85

Table 2 Specific surface area of BZ150, BZ550, and BZ850 samples

Sample	Specific surface area (m ² g ⁻¹)
BZ150	6.793
BZ550	5.743
BZ850	1.858

It is observed from FESEM study that the particle sizes are in the range of 50–500 nm. However, the crystallite sizes as calculated from the Scherrer equation are less than 34 nm. We need to resolve this apparent inconsistency. FESEM provides particle size. However, from Scherrer equation we get crystallite size. A crystallite is essentially a single crystal. Visible particles are seldom comprised of single crystallites except for some materials such as Si, Ge, some Ni based super-alloys *etc.* Generally, we deal with polycrystalline particles whereby a single particle is comprised of multiple crystallites, also known as grains in case of powder materials. Therefore, the particle size of a polycrystalline material would be bigger than the crystallite size. The presence of multiple peaks in the X-ray diffraction patterns of the samples reported in this work clearly suggests that all these samples are polycrystalline. Therefore, the particle sizes observed in FESEM images are much larger than the crystallite sizes calculated by Scherrer equation. However, with increasing crystallite size particle size definitely increases. The crystallite sizes of the samples increase from BZ150 to BZ850 and this suggests that particle size should also follow the same trend.

The coarsening of the nanoparticles with increasing annealing temperature was revealed by the BET study of BZ150, BZ550, and BZ850 (ref. ESI-Fig. II†). The specific surface areas of BZ150, BZ550, and BZ850 as derived from BET study are listed in Table 2.

BET specific surface area decreases marginally from BZ150 to BZ550. However, the BET specific surface area of BZ850 sample is considerably lower than that of BZ150 or BZ550 sample. This clearly suggests the onset of coarsening at higher temperatures. This result is also corroborated by FESEM images.

Fig. 4A(a)–(g) show the Raman spectra of all the samples in the wavenumber range of 0–3000 cm⁻¹. Group theory predicts that the Raman active zone-center optical phonons are A₁ + 2E₂ + E₁ + 2B₁. It is known that the B₁ mode is silent. The E₁ and A₁ modes are polar. They exhibit different frequencies for the transverse-optical (TO) and longitudinal-optical (LO) phonon modes. E₁ and A₁ are Raman active modes. The non-polar E₂ modes are Raman active and show two different frequencies *viz.* E₂ (high) and E₂ (low).^{31,32}

In Fig. 4A, for all the samples several peaks are visible. These peaks have been marked in the micro Raman spectra of BZ150 for facile understanding (ref. Fig. 4B). The exact peak positions are listed in ESI-Table 1.† The first five peaks (ref. Fig. 4B) can be ascribed to the E₂ (low), 2E₂ (low), A₁ (TO), E₂ (high), and E₁ (LO) modes, respectively.^{33,34} The peak at 1046 cm⁻¹ could not



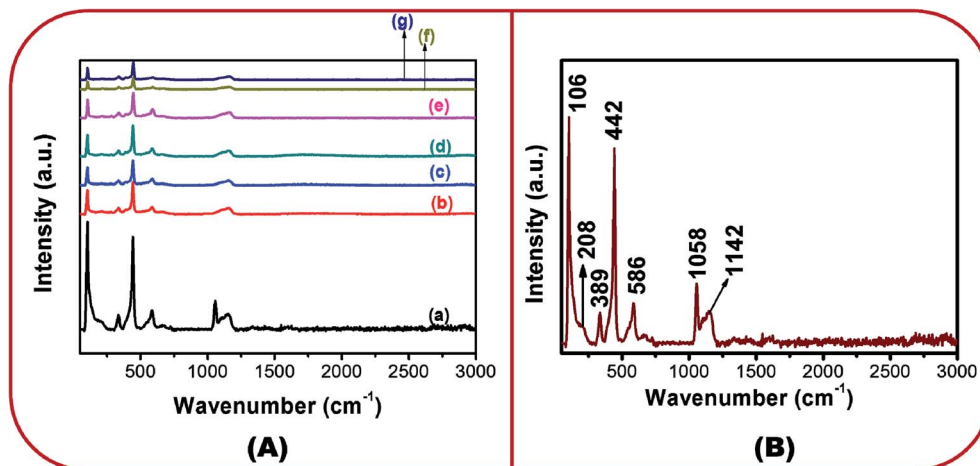


Fig. 4 (A) Micro-Raman spectra of (a) BZ150, (b) BZ350, (c) BZ450, (d) BZ550, (e) BZ650, (f) BZ750 and (g) BZ850 samples, and (B) marked micro-Raman spectra of BZ150.

be explained and the peak at $\sim 1150\text{ cm}^{-1}$ is ascribed to the E2 (LO) mode.³⁵

The peak at 104 cm^{-1} is due to the Zn ions.³³ The peak at 442 cm^{-1} is the band characteristic of wurtzite ZnO. Here, blue shifts of 3 cm^{-1} , 3 cm^{-1} , 5 cm^{-1} , 6 cm^{-1} , 5 cm^{-1} , 5 cm^{-1} , and 6 cm^{-1} have been observed with respect to the standard position of this peak (439 cm^{-1}) in BZ150, BZ350, BZ450, BZ550, BZ650, BZ750, and BZ850 samples, respectively. This may be attributed to the oxygen excess defects in the lattice.³⁵ A plausible mechanism has been proposed in a latter section in order to explain the inclusion of such oxygen excess defects.

The A1 (TO) mode is related to the crystallinity of ZnO.³⁶ Strong blue shiftings (19 cm^{-1} , 17 cm^{-1} , 20 cm^{-1} , 17 cm^{-1} , 22 cm^{-1} , 17 cm^{-1} , and 24 cm^{-1} in BZ150, BZ350, BZ450, BZ550, BZ650, BZ750, and BZ850 samples, respectively) of the peak

with respect to its standard position have been observed. Such significant blue shiftings in the peak position are suggestive of considerable anisotropy in the crystal structure of the samples. Such anisotropy might have originated from the oriented growth of the ZnO samples as shown in FESEM study (ref. Fig. 3). The peaks lying between $570\text{--}590\text{ cm}^{-1}$ are related to oxygen vacancy (V_{O}) and/or Zn_{i} defects.^{37,38} The possibility of the generation of V_{O} may be discarded owing to the use of oxygen rich precursor salt. Therefore, the peaks at $\sim 584\text{ cm}^{-1}$ may be ascribed to Zn_{i} defects.

Also, the 442 cm^{-1} peaks representing the O_{i} defects are far more intense than the respective $\sim 584\text{ cm}^{-1}$ peaks representing the Zn_{i} defects for all the samples. Thus, it is expected that the concentration of the O_{i} defects would be more than that of the Zn_{i} defects for all the samples. This has been further

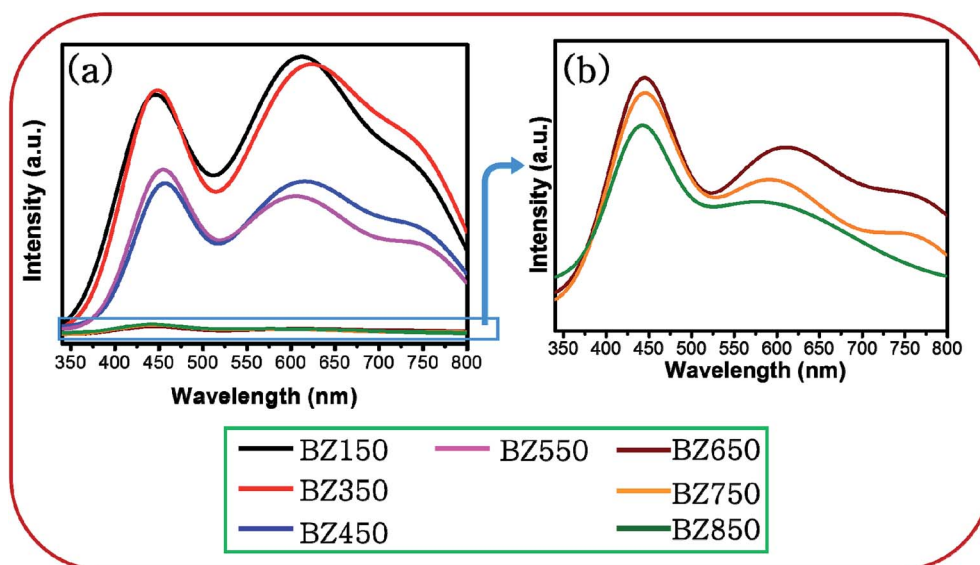


Fig. 5 (a) PL spectra of BZ150, BZ350, BZ450, BZ550, BZ650, BZ750 and BZ850 samples, and (b) zoomed PL spectra of BZ650, BZ750 and BZ850 samples.

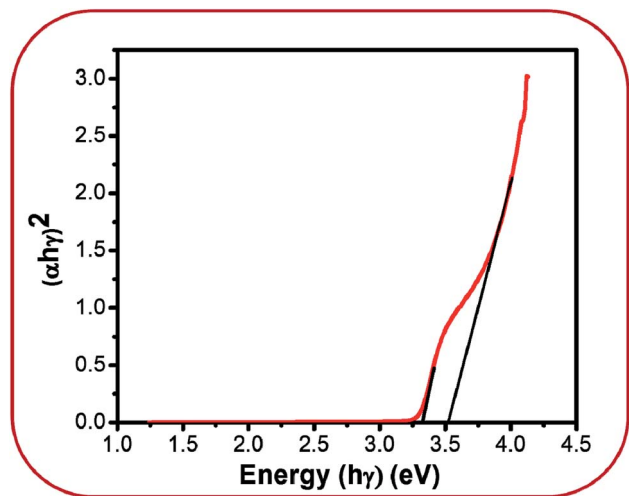


Fig. 6 UV-Vis plot of BZ150.

corroborated by the EDX study which clearly shows that the Zn/O ratio is less than 1 for all the samples (ref. ESI-Fig. 1 and Table 1†). The peak at $\sim 1150\text{ cm}^{-1}$ corresponds to the cationic and anionic defects.

Study of optical properties by photoluminescence (PL) and time resolved PL (τ -PL) spectroscopy

PL study. PL study of the as prepared samples were carried out to find out the defect states/bands formed by the different cationic and anionic defects formed in the crystal lattice. The excitation wavelength for all the samples was 320 nm and all the measurements were carried out at room temperature with same weight of the samples. The PL spectra of all the samples are shown in Fig. 5a. It is observed that the intensities of the PL emissions of BZ650, BZ750, and BZ850 are much lesser than those of the samples annealed at 150–550 °C. Therefore, zoomed PL spectra of these three samples have been shown in Fig. 5b.

Conventionally, PL spectra of ZnO show one peak in the UV region at $\sim 355\text{ nm}$ corresponding to the band to band transition.³⁹ However, the peaks in the UV region corresponding to band to band and band edge transitions are absent for all the samples. It seems plausible that the tail of the high intensity visible emissions near the band edge has masked such

emissions in the UV region. Since the intensities of the emissions in the UV region are inconsequential with respect to that of the visible emissions, these emissions will not be considered for further discussion.

However, band gap energy is essential information in explaining the origin of the visible emissions. UV-Vis analysis was conducted in order to get this information. Fig. 6 shows the UV-Vis plot for BZ150 sample. Two different energies, *viz.* 3.3 eV and 3.5 eV that are obtained from this plot can be attributed to excitonic transition⁴⁰ and band to band transition.³⁹ From these energy values the peak positions for excitonic and band to band transition are calculated as 375 nm and 355 nm, respectively. However, these peaks are not visible in the PL spectrum as mentioned earlier. Since the particle size of all the samples are much bigger than the Debye length for ZnO, it may be expected that the band gap of all the samples will be similar to that of BZ150, *viz.* $\sim 3.5\text{ eV}$.

The visible spectra of BZ150 to BZ750 samples can be deconvoluted into 3 peaks using Gaussian equation, whereas that of BZ850 sample can be deconvoluted into 2 such peaks. The peak positions and their respective intensities derived from the Gaussian fittings have been listed in Table 3.

Fig. 7 shows the deconvoluted PL peaks for all the samples. It is observed that, the first peaks of all the samples are narrow and centered around 430–450 nm causing blue emission (ref. Table 3). The peaks for all the samples lying between 430–450 nm are attributed to the direct recombination of photo-generated electrons trapped in the neutral and charged Zn_i defect states with the holes in the valence band.⁴¹ The oxygen rich precursors are believed to have triggered the formation of this defect.²⁴ Zn_i is a shallow donor level lying $\sim 0.4\text{ eV}$ below the conduction band.⁴² We believe that Zn_i and excited Zn_i (ex-Zn_i) form an almost continuous defect band designated as extended Zn_i band. Therefore, in all the samples the positions of blue emission peaks are slightly different from each other. Considering the fact that blue emission peaks of all the samples lie between 430–450 nm, we have calculated the width of the extended Zn_i band to be approximately 0.4 eV. This seems likely in view of the fact that in insulating materials such as MgO the width of point defect bands were found to be in the order of 1 eV.⁴³

From the above discussion it may be concluded that photo-generated electrons from conduction band take a non-radiative tour to the extended Zn_i defect band and thereafter jump to the

Table 3 PL peak positions for BZ150, BZ350, BZ450, BZ550, BZ650, BZ750, BZ850 and BZ950

Sample	Peak 1 (nm)	Intensity ($\times 10^6$)	Peak 2 (nm)	Intensity ($\times 10^6$)	Peak 3 (nm)	Intensity ($\times 10^6$)
BZ150	441	6.14	610	13.7	752	4.1
BZ350	444	5.63	619	13.8	755	4.31
BZ450	453	2.82	613	7.6	756	2.24
BZ550	451	3.2	605	7.17	758	2.0
BZ650	441	0.201	606	0.307	773	0.131
BZ750	441	0.195	591	0.267	766	0.079
BZ850	438	0.107	577	0.240	—	—



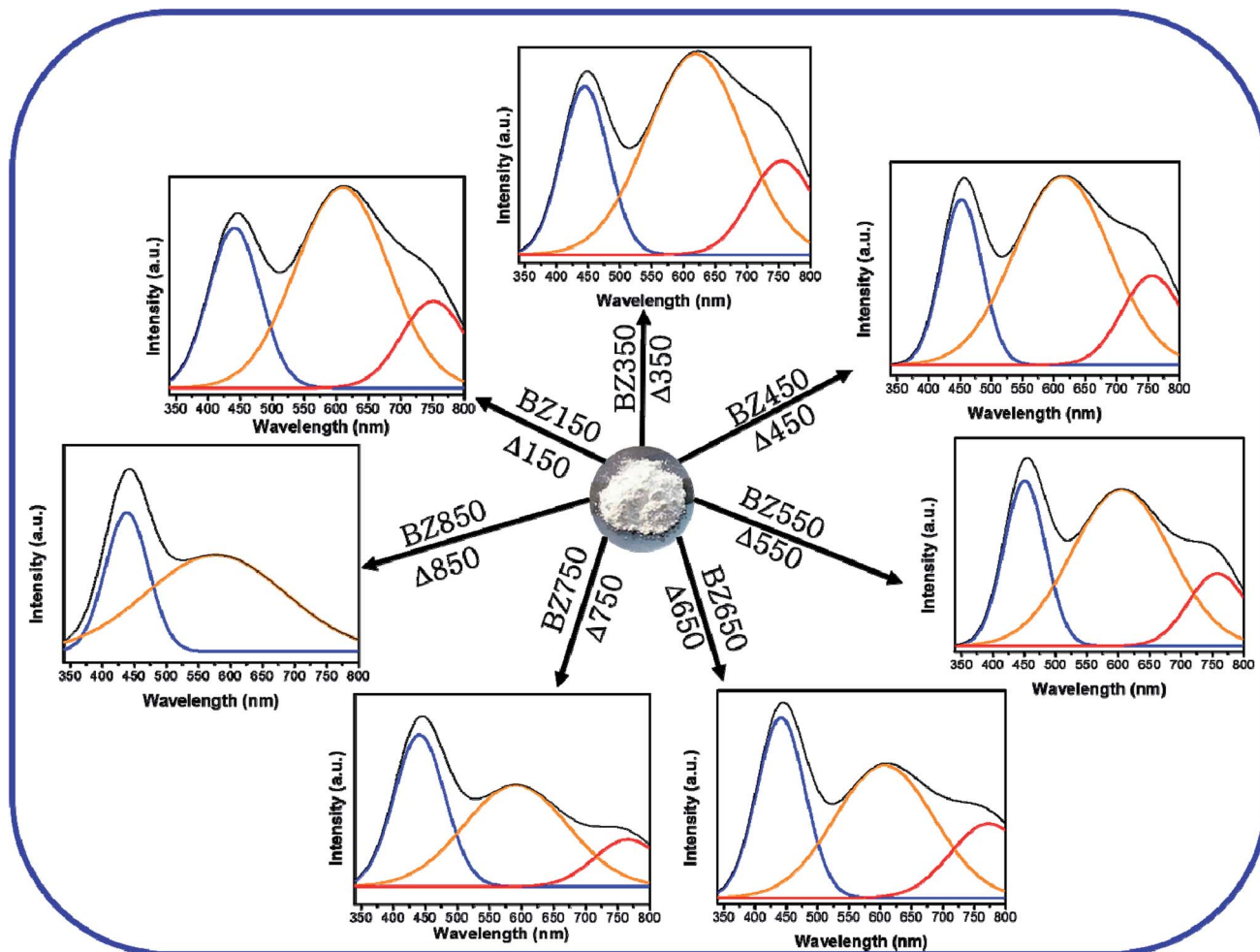


Fig. 7 Deconvoluted PL patterns of BZ150, BZ350, BZ450, BZ550, BZ650, BZ750, and BZ850 samples.

valence band with a blue emission to recombine with a hole. This is diagrammatically shown in Fig. 8.

For BZ150, BZ350, BZ450, BZ550, BZ650 and BZ750 samples the second peaks lie between 620–590 nm and cause yellow-orange emission (ref. Fig. 7 and Table 3). For BZ850 the second peak lies at 577 nm (ref. Fig. 7 and Table 3). The broad peaks lying in the region of 600–625 nm are attributed to the

neutral and charged O_i defects.²⁰ As discussed earlier, the presence of oxygen interstitial defects has also been established by Raman and EDX studies. The origin of this defect may be traced back to the oxygen rich precursors.²⁴ From literature it was found that, it is a deep-seated acceptor level lying 1.1 eV above the valence band.⁴² We believe that O_i along with excited O_i ($ex-O_i$) forms a defect band designated here as extended O_i

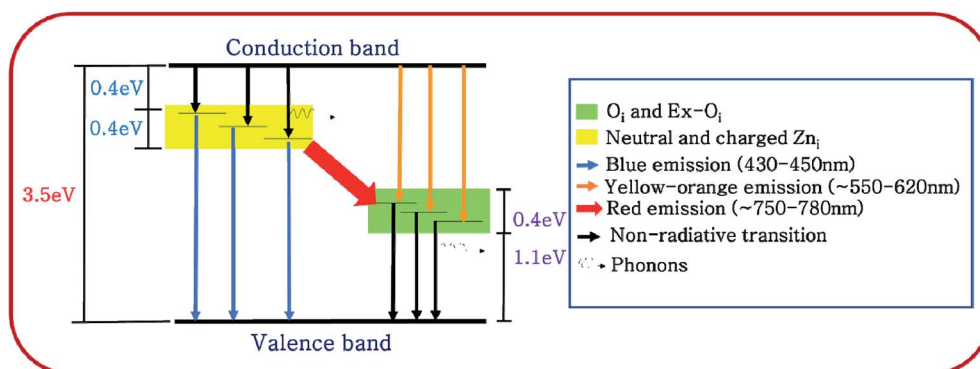


Fig. 8 Proposed band diagram of ZnO samples (BZ150–BZ850) including the defect bands.



band. Considering the fact that the yellow-orange emission peaks for all the samples lie between 550–620 nm, the width of the band is calculated to be ~ 0.4 eV and this seems logical considering the same fact that was taken into account while discussing the width of extended Zn_i band.⁴³ Photogenerated electrons in the conduction band recombines radiatively with the holes present in the extended O_i band, thereby giving rise to the yellow-orange emission (ref. Fig. 8). Since, this radiative recombination involves a defect band of substantial width instead of a particular defect state, there are sample to sample variations in the positions of the yellow orange emission peak centers. The electrons trapped in the extended O_i band travel to the valence band by a non-radiative transition (ref. Fig. 8).

With increasing annealing temperature, the concentration of the O_i and $ex-O_i$ defects reduce. Therefore, the width of the $ex-O_i$ defect band decreases, and the average energy gap between the defect band and conduction band increases. Therefore, the yellow-orange emission shifts towards higher energy side leading to a blue-shift in peak-2.

Finally, for BZ150, BZ350, BZ450, BZ550, BZ650 and BZ750 samples the third peaks lie between 750–780 nm and cause red emission. Plausibly, there is a non-radiative transition of the photogenerated electrons from the conduction band to the extended Zn_i band followed by a radiative transition to the extended O_i band causing red emission, and finally another non-radiative transition to valence band (ref. Fig. 8). In BZ150, BZ350, BZ450, BZ550, BZ650 and BZ750 samples the wavelength of red emission is such that it matches well with the energy difference of the extended Zn_i and extended O_i bands.

Additionally, it may be noted that for BZ850 sample the red emission is invisible. Fig. 5 clearly depicts that the intensity of all the emissions are decreasing with increasing annealing temperature *i.e.* defects are being gradually eliminated. It might be possible that in BZ850 sample the intensity of red emission has reduced to such an extent that the overwhelming tail of the yellow-orange emission has completely masked the red emission.

Peak-3 evolves as a result of transition of electrons from $ex-Zn_i$ defect band to $ex-O_i$ defect band. The minimum energy possible for this emission is 1.2 eV corresponding to an emission wavelength of ~ 1033 nm and the maximum energy possible is 2 eV corresponding to an emission wavelength of ~ 620 nm for BZ150 sample (ref. Fig. 8). However, at higher temperatures the $ex-O_i$ defect band shrinks and hence the minimum energy increases and consequently the wavelength possible for this emission shifts to ~ 885 nm. Since, at higher temperatures the emission in IR region significantly shifts towards the red region, more energies of higher wavelength emissions are added to peak-3. In other words, strong tails of IR emission(s) merge with peak-3. Thus, due to the increasing addition of energies of higher wavelengths to the red emission the peak at ~ 757 nm shifts towards higher wavelength (~ 775 nm). This explains the red shift of peak-3.

Annihilation of defect is a diffusion-controlled process. At lower annealing temperatures (150 °C and 350 °C) diffusion kinetics of the defects is slow and hence defects were not

annihilated significantly. Therefore, PL intensity did not change much from BZ150 to BZ350 sample.

However, at higher temperatures (above 350 °C) the rate of diffusion of the defects increases leading to a faster annihilation of the defects. Therefore, PL intensity reduced sharply from BZ350 to BZ450.

However, PL intensity did not reduce appreciably from BZ450 to BZ550. At higher temperatures rate of defect annihilation indeed increases. However, with increasing temperature the ionization of the neutral defects also increases. At lower temperatures the rate of ionization is negligible owing to unavailability of sufficient ionization energy. At sufficiently high temperatures ionization energy is available. However, at such high temperatures both ionized and neutral defects are annihilated owing to very high diffusivity. Therefore, PL intensity reduces sharply from BZ550 to BZ650.

The ionic lattice of ZnO poses an electrical potential field through which both neutral and ionized defects must move in order to diffuse to the surface. The ionized defects being charged species have stronger interaction with this field as compared to the neutral defects. Therefore, the activation energy barriers for the diffusion of these ionized defects are higher than those of neutral defects. At moderately high temperatures energy available is comparable to the activation energy barrier for the diffusion of neutral defects but is lower than that of the charged defects. Therefore, at such temperatures some of the neutral defects will be stabilized by ionization and hence rate of annihilation would reduce. This is what is observed at BZ550 as the PL intensity does not reduce comprehensively from BZ450 to BZ550.

Plausible mechanism for the formation of oxygen interstitial (O_i) and excited oxygen interstitial ($ex-O_i$). It may be noted that Zn_i defect is common place but O_i defect is relatively rare. Also, the generation of O_i involves high energy as it is a deep-seated defect level and hence it is bizarre that at such low synthesis temperature O_i defects will be formed. Here we have come up with a logical reaction mechanism for the generation of O_i defect states during the synthesis.

It is proposed that O_i and $ex-O_i$ defects form during the nucleation growth of ZnO from the precursor salt. Zinc nitrate,

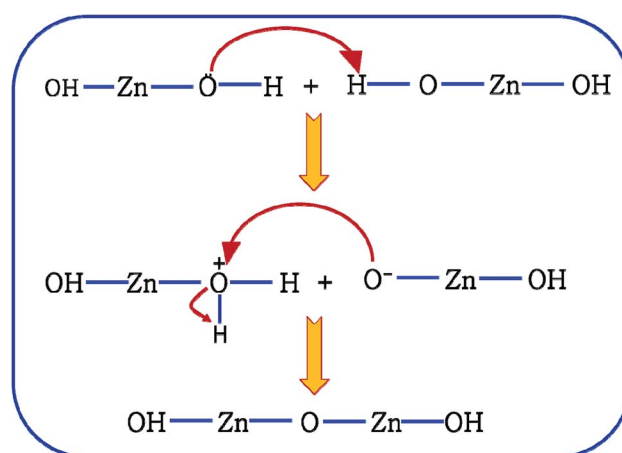


Fig. 9 Mechanism of condensation of $Zn(OH)_2$.



when refluxed in ammoniacal water (~ 10 pH) it initially produces zinc hydroxide with the chemical formula of $\text{Zn}(\text{OH})_2$. Oxygen atom in $\text{Zn}(\text{OH})_2$ has extra pair of electrons. Hence, O atom, a nucleophile from one $\text{Zn}(\text{OH})_2$ molecule attacks the H atom (electrophilic centre) of another $\text{Zn}(\text{OH})_2$ molecule in near proximity. This reaction involves the formation of two intermediate species *viz.* OH-Zn-O^- and $\text{H}_2\text{O}^+-\text{Zn-OH}$. The nucleophilic centre of OH-Zn-O^- (O^-) attacks the electrophilic centre (Zn) of $\text{H}_2\text{O}^+-\text{Zn-OH}$ leading to the elimination of one water molecule, leading to the condensation product of OH-Zn-O-Zn-OH . This reaction continues to form ZnO particles. This condensation process is schematically delineated in Fig. 9. This mechanism is an extension of the mechanism of water condensation of $\text{Si}(\text{OH})_4$ to form $-\text{Si-O-Si}-$ under basic condition.⁴⁴

This mechanism is now further extended to explain the presence of O_i and ex-O_i defects in the precipitate. During nucleation and growth phase lots of OH^- are available owing to highly basic condition and the O atoms in that behave as nucleophiles. At the same time the Zn ion of the condensation product, OH-Zn-O-Zn-OH attains partial positive charge as its electron clouds shift towards the adjacent O atoms having high electronegativity. These Zn atoms behave like electrophilic centres and get attacked by the nucleophilic oxygen atom of a hydroxyl ion, thereby forming a weak electrostatic bond amongst them. This scenario is schematically depicted in the first step of Fig. 10a. Nucleophilic oxygen of one such weakly bonded hydroxyl ion attacks the hydrogen atom of another such hydroxyl ion in the vicinity to form an intermediate species. This species then loses the water molecule. The doubly charged oxygen atom shown in the third step of Fig. 10a will be found in the final ZnO lattice as O''_i . The size of oxygen atom is very small, the precipitation of ZnO involves nucleation and growth, and nuclei are extremely small in size providing very high surface areas. Therefore, it is plausible that a myriad of such O''_i will get entrapped in the ZnO lattice during the nucleation and growth stage. Also due to the small size of the nuclei during

precipitation, there would be a substantial amount of Zn terminated species such as, $\text{Zn}^+-\text{O-Zn-OH}$ *etc.* Such species will lead to the formation of O'_i and O_i as shown in Fig. 10b and c, respectively. Thus, the above is the plausible mechanism for the generation of very large concentrations of O_i and ex-O_i defects during precipitation of ZnO.

Plausible mechanism for the formation of zinc interstitial (Zn_i) and excited zinc interstitial (ex-Zn_i). The size of the Zn^{2+} (0.74 Å) is smaller than O^{2-} (1.42 Å). Secondly, during precipitation of ZnO nuclei formed are extremely small and consequently highly energetic. Being smaller, the energy barrier of migration of Zn^{2+} to the interstitial sites would be small and secondly nuclei being highly energetic, effective energy barrier would further be reduced than that of the bulk. Thus, one would expect the formation of more of Zn_i by Frenkel mechanism during the course of precipitation *via* the nucleation growth process. Subsequently, Zn_i could be ionized to form ex-Zn_i . Thus the mechanism of generation of Zn_i and ex-Zn_i could be represented as follows:



The transition of one or two electrons from Zn_i to the conduction band gives rise to Zn_i^+ and Zn_i^{++} , and can be given by,



Determination of CIE-coordinates and corresponding correlated colour temperature (CCT). The CIE plots of all the samples from BZ150 to BZ850 are shown in Fig. 11. The corresponding chromaticity coordinates (X, Y) are tabulated in Table 4. These coordinates were used to calculate the correlated colour temperature (CCT) of all the samples following McCamy's relation,⁴⁵ given by, $\text{CCT} = 449n^3 + 3525n^2 + 6823.3n + 5520.3$, where $n = (X - 0.3320)/(0.1858 - Y)$. The correlated colour

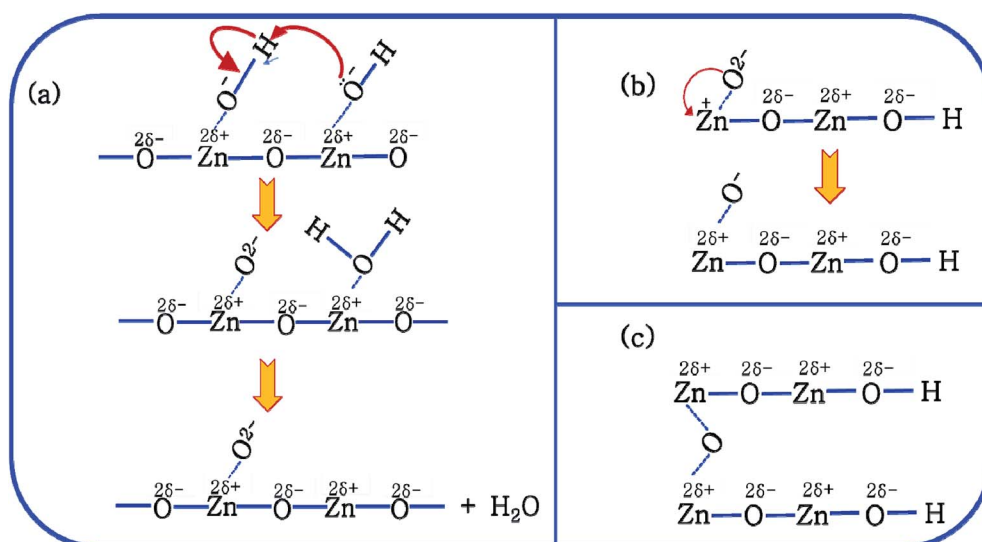


Fig. 10 Mechanism of formation of (a) O''_i , (b) O'_i and (c) O_i .



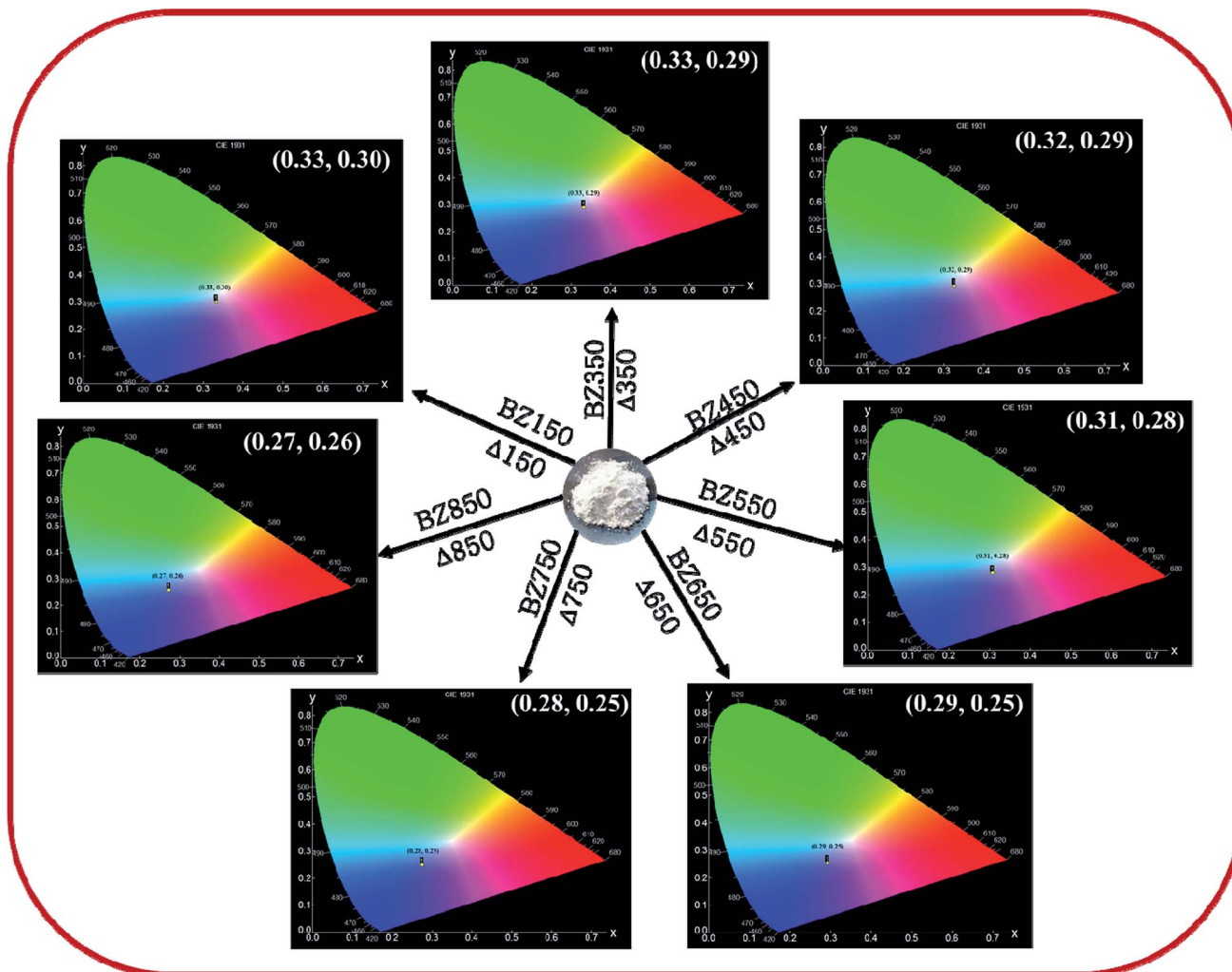


Fig. 11 CIE plots of BZ150, BZ350, BZ450, BZ550, BZ650, BZ750, and BZ850 samples.

temperatures (CCT) (ref. Table 4) ensure that the emissions corresponding to all the samples are cool in nature as all the CCT values are more than 4000 K. This result is important as in LED based applications cool light is preferred.

Whereas, the chromaticity co-ordinates of BZ150, BZ350 and BZ450 sit on the edge of the white spot in the CIE plot, chromaticity co-ordinates of BZ550, BZ650, BZ750, and BZ850 are clearly blue shifted. Fig. 12a shows that annealing of the as prepared ZnO sample at various temperatures from 150 °C to

Table 4 CIE co-ordinates and CCT values of BZ150, BZ350, BZ450, BZ550, BZ650, BZ750, and BZ850 samples

Sample	X	Y	CCT (K)
BZ150	0.33	0.30	5641
BZ350	0.33	0.29	5651
BZ450	0.32	0.29	6352
BZ550	0.31	0.28	7311
BZ650	0.29	0.25	11 616
BZ750	0.28	0.25	13 585
BZ850	0.27	0.26	13 936

850 °C in ordinary air atmosphere causes the intensity of yellow-orange emission to reduce at a much faster rate than that of blue emission. Hence, it might be expected that the CIE co-ordinates will be blue shifted and exactly that has happened. The reason for faster decay of yellow-orange emission with respect to blue emission can be explained with the diffusion kinetics of O_i and Zn_i defects.

Evidently, with increasing temperature of annealing the O_i defect responsible for yellow-orange emission is annihilated at a much faster rate than the Zn_i defect responsible for the blue emission. The activation energy barrier to diffusion of Zn_i (Q_{Zn_i}) is only about 0.3–0.5 eV.^{46–48} Since the size of O^{2-} (1.42 Å) is much bigger than that of Zn^{2+} (0.74 Å), it might be expected that the activation energy barrier to the diffusion of oxygen interstitial (Q_{O_i}) is higher than Q_{Zn_i} . The temperature dependent variation of diffusion coefficient of O_i ($D(O_i)$) and Zn_i ($D(Zn_i)$) would be given by,

$$D(O_i) = D_0(O_i)e^{-\frac{Q_{O_i}}{kT}} \quad (3)$$

$$D(Zn_i) = D_0(Zn_i)e^{-\frac{Q_{Zn_i}}{kT}} \quad (4)$$



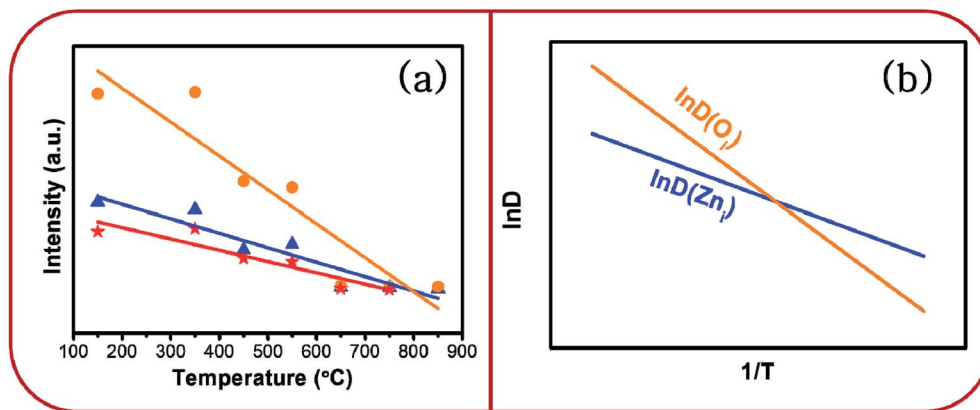


Fig. 12 (a) Dependence of PL intensity of ZnO samples on annealing temperature and (b) schematic plot of $\ln D$ vs. $1/T$.

Fig. 12b gives the schematic plot of $\ln D$ vs. $1/T$.

From the plot it is observed that $\ln D(O_i)$ increases at a much faster rate than $\ln D(Zn_i)$ with the increase in temperature. Therefore, diffusion flux $J(O_i)$ would increase at a much faster rate than $J(Zn_i)$ with increasing temperature. Therefore, the O_i defects would be annealed much faster than the Zn_i defects, especially at higher temperatures. This is observed in Fig. 12a.

However, this analysis does not answer the question why high temperature annealing under ordinary atmosphere reduces the intensity of the oxygen interstitial defects. It has already been explained in an earlier section that O_i and charged O_i was generated by a non-equilibrium process during the precipitation of ZnO by the process of nucleation. Now if this O_i concentration was to be in equilibrium with the partial pressure of oxygen, p_{O_2} according to the following equation:



then equilibrium partial pressure oxygen $p_{O_2}^{eq}$ would be given by,

$$p_{O_2}^{eq} = \frac{[O_i]^2}{K^2} \quad (6)$$

where K is the equilibrium constant of eqn (6). Since, as discussed earlier $[O_i]$ is much higher during the precipitation therefore, $p_{O_2}^{eq} \gg p_{O_2}$. Therefore, eqn (5) should be driven in the backward direction in order to achieve $p_{O_2}^{eq}$. However, at lower

temperature this $[O_i]$ is stabilized by slow kinetics of diffusion. When the samples are heat treated in ordinary atmosphere at higher temperatures the diffusion kinetics of O_i becomes sufficiently fast resulting in the decrease of the $[O_i]$. Increasing temperature will enhance this process exponentially (ref. eqn (3)), thereby accounting for the drastic fall in the intensity of the O_i . Similar argument will be held true for ex- O_i . The decrease in the intensity of blue emission due to Zn_i and ex- Zn_i defects as a function of heat treatment of the samples at higher temperature in ordinary atmosphere could also be explained by similar arguments as delineated above.

τ -PL study. The time decay plots of the blue and yellow-orange emissions for all the samples are shown in Fig. 13a and b, respectively. The experimental time decay plots could be fitted well with an exponential decay equation of two orders suggesting that there are two different paths for the photo-generated electrons to decay, *viz.* reductive recombination and non-radiative recombination. The two-order decay equation is given by,

$$R(t) = A + B_1 e^{-t/\tau_1} + B_2 e^{-t/\tau_2}, \quad (7)$$

where $R(t)$ is the intensity of the decaying emission at an instant t , A is a constant, B_1 and B_2 are the amplitudes of non-radiative and radiative recombination, respectively, and τ_1 and τ_2 are non-radiative and radiative recombination times, respectively.

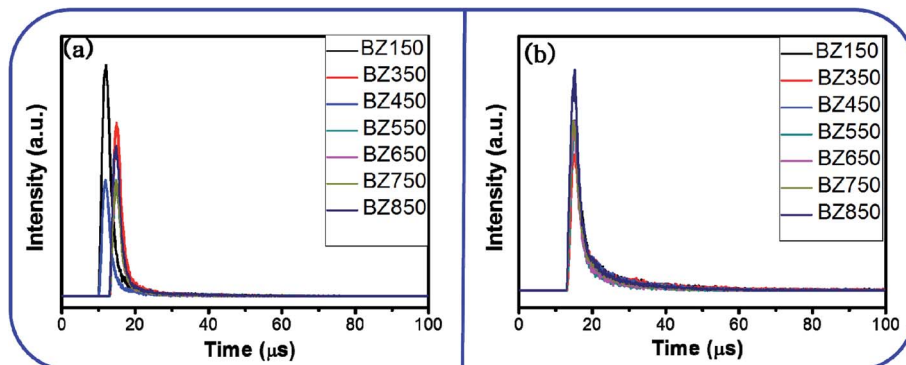


Fig. 13 Time decay plots of the (a) the blue emission and (b) the yellow-orange emission of the BZ150, BZ350, BZ450, BZ550, BZ650, BZ750, and BZ850 samples.



Table 5 Decay times of BZ150, BZ350, BZ450, BZ550, BZ650, BZ750, and BZ850 samples for the blue emission

Sample	Blue (nm)	τ_1 (μ s)	B_1	τ_2 (μ s)	B_2	QY (%)
BZ150	441	1.367	2208.197	9.128	129.760	13.0
BZ350	444	1.433	1741.3	10.0	82.630	12.53
BZ450	453	1.382	1139.285	9.533	64.850	12.66
BZ550	451	1.414	1129.059	11.64	56.410	10.83
BZ650	441	1.35	1139.646	9.643	56.071	12.28
BZ750	441	1.35	1112.056	10.0	50.849	11.89
BZ850	438	1.312	1461.115	10.0	68.224	11.6

The non-radiative and radiative recombination times and their respective amplitudes derived from these fittings are tabulated in Tables 5 and 6. All the decay times for all the samples are in the microsecond order. Hence all the samples can be considered as phosphors.

The average decay time periods of the blue emissions for BZ150, BZ350, BZ450, BZ550, BZ650, BZ750, and BZ850 samples are calculated as 3.55 μ s, 3.56 μ s, 3.68 μ s, 4.4 μ s, 3.51 μ s, 3.54 μ s, and 3.59 μ s, respectively. Similarly, the average decay time periods of the yellow-orange emissions of BZ150, BZ350, BZ450, BZ550, BZ650, BZ750, and BZ850 samples are computed as 8.9 μ s, 9.13 μ s, 7.27 μ s, 5.49 μ s, 5.43 μ s, 6.29 μ s, and 6.26 μ s, respectively. However, decay time periods for the red emission could not be determined as the intensity of the red emission was too low. It is to be noted that the integrated PL intensities of blue and red emissions (ref. Table 3) are comparable. However, the peak for blue emission is sharp and tall whereas the peak for red emission is diffused and short. Therefore, the peak intensity at the center of the peak is much higher for the blue emissions as compared to the red emissions. Time resolved PL is measured at the center of the peaks only. Therefore, τ -PL for blue emission could be measured whereas that of red emission could not be.

Calculation of quantum yield. The quantum yields (QY) of the samples were calculated using the following equation,

$$QY = \frac{\frac{1}{\tau_2}}{\frac{1}{\tau_1} + \frac{1}{\tau_2}} \quad (8)$$

The QYs of the samples for the blue emissions and yellow-orange emissions are tabulated in Tables 5 and 6, respectively.

Table 6 Decay times of BZ150, BZ350, BZ450, BZ550, BZ650, BZ750, and BZ850 samples for the yellow-orange emission

Sample	Yellow-orange (nm)	τ_1 (μ s)	B_1	τ_2 (μ s)	B_2	QY (%)
BZ150	610	1.151	553.147	11.86	142.21	8.84
BZ350	619	1.707	630.283	14.1	114.04	10.79
BZ450	614	1.326	700.916	10.63	154.32	9.42
BZ550	605	1.41	952.777	9.445	146.956	12.9
BZ650	606	1.595	906.816	10	121.512	13.75
BZ750	591	1.67	936.85	10.15	184.4	14.12
BZ850	577	1.434	1089.387	10	202.128	12.54

These QY values are comparable to those of the ZnO based materials reported earlier, *viz.* 15–21% in solid ZnO quantum dots,⁴⁹ 3–5% in ZnO quantum dots dispersed in ethanol,⁵⁰ 1.6% corresponding to the excitonic emission in bulk ZnO,⁵¹ 12.7–15.2% corresponding to the visible emission in bulk ZnO¹⁵ *etc.*

Defects (Zn_i , O_i *etc.*) act as trap states for photogenerated electrons. Photogenerated electrons are trapped in those defect states. Eventually, those electrons recombine with the holes, both by radiative and non-radiative means. Consequently, there would be radiative and non-radiative recombination times given by τ_2 and τ_1 , respectively. Now, eqn (8) clearly suggests that τ_2 and τ_1 determine the QY and these parameters may or may not vary with PL intensity. It should be noted that in this case annealing temperature has prominent effect on PL intensity (ref. Table 3) but negligible effect on τ_2 and τ_1 (ref. Tables 5 and 6). That is why QY here remains nearly unchanged irrespective of PL intensity.

The nanoparticles reported in here are mostly large in size which is corroborated by both FESEM and BET studies. This has an important implication on the long-term stability of the phosphorescence reported herein. It has already been stated that defect annihilation is a diffusion-controlled process and the defects (O_i and Zn_i) have to diffuse to the surface of the nanoparticles in order to get annihilated. Owing to the large particle size the diffusion length becomes very high. Therefore, the rate of defect annihilation reduces greatly. Further, the rate of defect annihilation is negligible in all the annealed samples (BZ150 to BZ850) at room temperature because low thermal energy is available at room temperature. This in turn would ensure the long-term stability of the defect mediated PL.

Conclusions

In summary, we have systematically studied the effect of annealing temperature on the blue phosphorescence in ZnO nanopowder. ZnO nanopowder was prepared by a facile, and cost-effective solution-precipitation method. The prepared nanopowders annealed at different temperatures were characterized by XRD, FESEM, EDX, BET, and micro-Raman spectroscopy to have an insight into the microstructure of the material. Photoluminescence emission spectra of these samples revealed the presence of blue, yellow, and red components originating from crystalline point defects, *viz.* zinc interstitial (Zn_i), and oxygen interstitial (O_i). A mechanism explaining the origin of such defects has been proposed. The concentrations of these defects and the intensity of the corresponding PL emission peaks varied as a function of annealing temperature. The corresponding CIE plots revealed that the overall color of emission gradually turned from light blue (CIE co-ordinate: (0.33, 0.30)) to dark blue (CIE co-ordinate: (0.27, 0.26)) as the annealing temperature increased from 150 °C to 850 °C. A thermodynamic interpretation to such variance in defect concentration has been proposed. τ -PL study and correlated color temperature (CCT) calculations ensured phosphorescence (decay time \sim 9–12 μ s) and cool lighting (CCT \sim 5000–14 000 K) in all the samples. Finally, all the samples exhibited comparable quantum yields with respect to previous ZnO based



phosphorescence reports. This study suggests that thermal annealing can potentially be a technique for precise tuning of defect-mediated phosphorescence.

Funding sources

This research did not receive any specific grant from funding agencies in the public, commercial, or not-for-profit sectors.

Conflicts of interest

There are no conflicts of interest to declare.

Acknowledgements

The authors are greatly indebted to Dr G. C. Das, Ex-Professor, Department of Metallurgical and Material Engineering, for helpful discussions. The authors acknowledge the instrumental facilities obtained from the Department of Metallurgical and Materials Engineering and School of Materials Science and Nanotechnology, Jadavpur University. The authors are also thankful to Dr Somnath Bandyopadhyay, Head, Functional Materials and Devices Division for extending moral support. The authors gratefully acknowledge the kind support of Director, CSIR-Central Glass and Ceramic Research Institute, Kolkata.

References

- 1 M. Qiao, B. Zhang, Z. Xiao, J. Fang, and Z. Li, *Power Semiconductor Devices and IC's, ISPSD '08. 20th International Symposium*, 18–22 May 2008, p. 52.
- 2 A. Morell and N. El Khiati, Green Phosphors for Large Plasma TV Screens, *J. Electrochem. Soc.*, 1993, **140**, 2019–2022.
- 3 N. Hirosaki, R.-J. Xie, K. Inoue, T. Sekiguchi, B. Dierre and K. Tamura, Blue-emitting AlN: Eu²⁺ nitride phosphor for field emission displays, *Appl. Phys. Lett.*, 2007, **91**, 061101_1–061101_3.
- 4 M. Leskela, Rare earths in electroluminescent and field emission display phosphors, *J. Alloys Compd.*, 1998, **275–277**, 702–708.
- 5 H. Kamikubo, ZnO: Zn phosphor for vacuum fluorescent display, *US Pat.* 5128063A, Nec Corporation, Japan, 1992.
- 6 H. Morkoc, *Nitride Semiconductor Devices: Fundamentals and Applications*, Wiley-VCH, Weinheim, Germany 2013, ch. 7.
- 7 W. W. Holloway and M. Kestigian, Optical Properties of Cerium-Activated Garnet Crystals, *J. Opt. Soc. Am.*, 1969, **59**, 60–63.
- 8 J. M. Robertson, M. W. van Tol, W. H. Smits and J. P. H. Heynen, Colourshift of the Ce³⁺ emission in monocrystalline epitaxially grown garnet layers, *Philips J. Res.*, 1981, **36**(1), 15–30.
- 9 I. Provencio, I. R. Rodriguez, G. Jiang, W. P. Haye, E. F. Moreira and M. D. Rollag, A novel human opsin in the inner retina, *J. Neurosci.*, 2000, **20**(2), 600–605.
- 10 K. Thapan, J. Arendt and D. J. Skene, An action spectrum for melatonin suppression: evidence for a novel non-rod, non-cone photoreceptor system in humans, *J. Physiol.*, 2001, **535**(1), 261–267.
- 11 Z. C. Wu, J. X. Shi, J. Wang, M. L. Gong and Q. Su, A novel blue-emitting phosphor LiSrPO₄:Eu²⁺ for white LEDs, *J. Solid State Chem.*, 2006, **179**, 2356–2360.
- 12 Z. C. Wu, J. X. Shi, J. Wang, H. Wu, Q. Su and M. L. Gong, Synthesis and luminescent properties of SrAl₂O₄:Eu²⁺ green-emitting phosphor for white LEDs, *Mater. Lett.*, 2006, **60**, 3499–3501.
- 13 S. H. M. Poort, W. Janssen and G. Blasse, Optical properties of Eu²⁺-activated orthosilicates and orthophosphates, *J. Alloys Compd.*, 1997, **260**, 93–97.
- 14 J. K. Park, K. J. Choi, J. H. Yeon, S. J. Lee and C. H. Kim, Embodiment of the warm white-light-emitting diodes by using a Ba²⁺ codoped Sr₃SiO₅:Eu phosphor, *Appl. Phys. Lett.*, 2006, **88**, 043511_1–043511_3.
- 15 Y. Dai, Y. Zhang, Q. K. Li and C. W. Nan, Synthesis and optical properties of tetrapod-like zinc oxide nanorods, *Chem. Phys. Lett.*, 2002, **358**, 83–86.
- 16 N. K. Zayer, R. Greef, K. Rogers, A. J. C. Grellier and C. N. Pannell, In situ monitoring of sputtered zinc oxide films for piezoelectric transducers, *Thin Solid Films*, 1999, **352**, 179–184.
- 17 Ü. Özgür, Y. I. Alivov, C. Liu, A. Teke, M. A. Reshchikov, S. Dögan, V. Avrutin, S.-J. Cho and H. Morkoç, A Comprehensive Review of ZnO Materials and Devices, *J. Appl. Phys.*, 2005, **98**, 041301.
- 18 T. M. Børseth, B. G. Svensson and A. Y. Kuznetsov, Identification of oxygen and zinc vacancy optical signals in ZnO, *Appl. Phys. Lett.*, 2006, **89**, 262112_1–262112_3.
- 19 N. S. Parmar, L. A. Boatner, K. G. Lynn and J.-W. Choi, Zn Vacancy Formation Energy and Diffusion Coefficient of CVT ZnO Crystals in the Sub-Surface Micron Region, *Sci. Rep.*, 2018, **8**, 13446_1–13446_8.
- 20 L. E. Greene, M. Law, J. Goldberger, F. Kim, J. C. Johnson, Y. Zhang, R. J. Saykally and P. Yang, Low-temperature wafer-scale production of ZnO nanowire arrays, *Angew. Chem.*, 2003, **115**, 3139–3142.
- 21 M. Liu, A. H. Kitai and P. Mascher, Point defects and luminescence centres in zinc oxide and zinc oxide doped with manganese, *J. Lumin.*, 1992, **54**, 35–42.
- 22 X. L. Wu, G. G. Siu, C. L. Fu and H. C. Ong, Photoluminescence and cathodoluminescence studies of stoichiometric and oxygen-deficient ZnO films, *Appl. Phys. Lett.*, 2001, **78**, 2285–2287.
- 23 S. A. Studenikin, N. Golego and M. Cocivera, Fabrication of green and orange photoluminescent, undoped ZnO films using spray pyrolysis, *J. Appl. Phys.*, 1998, **84**, 2287–2294.
- 24 A. A. Sokol, S. A. French, S. T. Bromley, C. R. A. Catlow, H. J. J. van Dam and P. Sherwood, Point defects in ZnO, *Faraday Discuss.*, 2007, **134**, 267–282.
- 25 E. Rauwel, A. Galeckas, P. Rauwel, M. F. Sunding and H. Fjellvaag, Precursor-dependent blue-green photoluminescence emission of ZnO nanoparticles, *J. Phys. Chem. C*, 2011, **115**(51), 25227–25233.



- 26 Y. Gong, C. Zou, Y. Yao, *et al.*, A facile approach to synthesize rose-like ZnO/reduced graphene oxide composite: fluorescence and photocatalytic properties, *J. Mater. Sci.*, 2014, **49**(16), 5658–5666.
- 27 G. Singh, A. Choudhary, D. Haranath, *et al.*, ZnO decorated luminescent graphene as a potential gas sensor at room temperature, *Carbon*, 2012, **50**(2), 385–394.
- 28 A. B. Djurišić, Y. H. Leung, K. H. Tam, L. Ding, W. K. Ge, H. Y. Chen and S. Gwo, Green, yellow, and orange defect emission from ZnO nanostructures: Influence of excitation wavelength, *Appl. Phys. Lett.*, 2006, **88**, 103107.
- 29 W. C. Zhang, X. L. Wu, H. T. Chen, J. Zhu and G. S. Huang, Excitation wavelength dependence of the visible photoluminescence from amorphous ZnO granular films, *J. Appl. Phys.*, 2008, **103**, 093718.
- 30 C. R. Garcia, J. Oliva, L. A. Diaz-Torres, E. Montes, G. Hirata, J. Bernal Alvarado and C. Gomez-Solis, Controlling the white phosphorescence ZnGa₂O₄ phosphors by surface defects, *Ceram. Int.*, 2019, **45**(4), 4972–4979.
- 31 N. Ashkenov, B. N. Mbenkum, C. Bundesmann, V. Riede, M. Lorenz, D. Spemann, E. M. Kaidashev, A. Kasic, M. Schubert and M. Grundmann, Infrared dielectric functions and phonon modes of high-quality ZnO films, *J. Appl. Phys.*, 2003, **93**, 126–133.
- 32 J. F. Scott, UV Resonant Raman Scattering in ZnO, *Phys. Rev. B: Solid State*, 1970, **2**, 1209–1211.
- 33 H. Fukushima, T. Kozu, H. Shima, H. Funakubo, H. Uchida, T. Katoda and K. Nishida, *Joint IEEE International Symposium on the Applications of Ferroelectric, International Symposium on Integrated Functionalities and Piezoelectric Force Microscopy Workshop (ISAF/ISIF/PFM)*, 24–27 May 2015.
- 34 J. Wang, S. Hou, H. Chen and L. Xiang, Defects-Induced Room Temperature Ferromagnetism in ZnO Nanorods Grown from ϵ -Zn(OH)₂, *J. Phys. Chem. C*, 2014, **118**, 19469–19476.
- 35 J. Das, S. K. Pradhan, D. R. Sahu, D. K. Mishra, S. N. Sarangi, B. B. Nayak, S. Verma and B. K. Roul, Micro-Raman and XPS studies of pure ZnO ceramics, *Phys. B*, 2010, **405**, 2492–2497.
- 36 S. Vempati, A. Shetty, P. Dawson, K. Nanda and S. B. Krupanidhi, Cobalt-doped ZnO nanowires on quartz: synthesis by simple chemical method and characterization, *J. Cryst. Growth*, 2012, **343**(1), 7.
- 37 R. Cusco, E. A. Llado, J. Ibáñez, L. Artús, J. Jiménez, B. Wang and M. J. Callahan, Temperature dependence of Raman scattering in ZnO, *Phys. Rev. B: Condens. Matter Mater. Phys.*, 2007, **75**, 165202-1–165202-11.
- 38 S. H. Jeong, J. K. Kim and B. T. Lee, Effects of growth conditions on the emission properties of ZnO films prepared on Si (100) by rf magnetron sputtering, *J. Phys. D: Appl. Phys.*, 2003, **36**, 2017–2020.
- 39 S. Das, U. K. Ghorai, R. Dey, C. K. Ghosh and M. Pal, Novel multiple phosphorescence in nanostructured zinc oxide and calculations of correlated colour temperature, *Phys. Chem. Chem. Phys.*, 2017, **19**, 22995–23006.
- 40 Z. Jia, L. Yue, Y. Zheng and Z. Xu, Rod-like zinc oxide constructed by nanoparticles: synthesis, characterization and optical properties, *Mater. Chem. Phys.*, 2008, **107**, 137–141.
- 41 H. Zeng, G. Duan, Y. Li, S. Yang, X. Xu and W. Cai, Blue Luminescence of ZnO Nanoparticles Based on Non-Equilibrium Processes: Defect Origins and Emission Controls, *Adv. Funct. Mater.*, 2010, **20**(4), 561–572.
- 42 X. Liu, X. Xing, Y. Li, N. Chen, I. Djerdj and Y. Wang, Controllable synthesis and change of emission color from green to orange of ZnO quantum dots using different solvents, *New J. Chem.*, 2015, **39**, 2881–2888.
- 43 W. D. Kingery, H. K. Bowen and D. R. Uhlmann, *Introduction to Ceramics*, Wiley-Interscience Publications, NY, 2nd edn, 1975.
- 44 C. J. Brinker and G. W. Scherer, *Sol-Gel Science: The Physics and Chemistry of Sol-Gel Processing*, Elsevier Publications, 1st edn, 2013.
- 45 M. Rai, G. Kaur, S. K. Singh and S. B. Rai, Probing a new approach for warm white light generation in lanthanide doped nanophosphors, *Dalton Trans.*, 2015, **44**, 6184–6192.
- 46 G.-Y. Huang, C.-Y. Wang and J.-T. Wang, First-principles study of diffusion of zinc vacancies and interstitials in ZnO, *Solid State Commun.*, 2009, **149**, 199–204.
- 47 P. Erhart and K. Albe, Diffusion of zinc vacancies and interstitials in zinc oxide, *Appl. Phys. Lett.*, 2006, **88**, 201918_1–201918_3.
- 48 A. Janotti and C. G. Van de Walle, Native point defects in ZnO, *Phys. Rev. B: Condens. Matter Mater. Phys.*, 2007, **76**, 165202_1–165202_22.
- 49 S. Das, C. K. Ghosh, R. Dey and M. Pal, Novel green phosphorescence from pristine ZnO quantum dots: tuning of correlated color temperature, *RSC Adv.*, 2016, **6**, 236.
- 50 D. Bera, L. Qian, S. Sabui, S. Santra and P. H. Holloway, Photoluminescence of ZnO quantum dots produced by a sol-gel process, *Opt. Mater.*, 2008, **30**, 1233–1239.
- 51 N. S. Norberg and D. R. Gamelin, Influence of Surface Modification on the Luminescence of Colloidal ZnO Nanocrystals, *J. Phys. Chem. B*, 2005, **109**, 20810–20816.

